University of Pennsylvania
ScholarlyCommons

Departmental Papers (MSE) | Department of Materials Science & Engineering

December 2002

Potential and Impedance Imaging of Polycrystalline $BiFeO_3$ Ceramics

Sergei V. Kalinin
University of Pennsylvania

Matthew R. Suchomel
University of Pennsylvania

Peter K. Davies
University of Pennsylvania, davies@lrsm.upenn.edu

Dawn A. Bonnell
University of Pennsylvania, bonnell@lrsm.upenn.edu

Follow this and additional works at: http://repository.upenn.edu/mse_papers

Recommended Citation
Kalinin, S. V., Suchomel, M. R., Davies, P. K., & Bonnell, D. A. (2002). Potential and Impedance Imaging of Polycrystalline $BiFeO_3$ Ceramics. Retrieved from http://repository.upenn.edu/mse_papers/31

Copyright The American Ceramic Society. Reprinted from *Journal of the American Ceramic Society*, Volume 85, Issue 12, December 2002, pages 3011-3017.

This paper is posted at ScholarlyCommons. http://repository.upenn.edu/mse_papers/31
For more information, please contact libraryrepository@pobox.upenn.edu.

Potential and Impedance Imaging of Polycrystalline $BiFeO_3$ Ceramics

Abstract
Electrostatic-force-sensitive scanning probe microscopy (SPM) is used to investigate grain boundary behavior in polycrystalline $BiFeO_3$ ceramics. Scanning surface potential microscopy (SSPM) of a laterally biased sample exhibits potential drops due to resistive barriers at the grain boundaries. In this technique, the tips acts as a moving voltage probe detecting local variations of potential associated with the ohmic losses within the grains and at the grain boundaries. An approach for the quantification of grain boundary, grain interior, and contact resistivity from SSPM data is developed. Scanning impedance microscopy (SIM) is used to visualize capacitive barriers at the grain boundaries. In SIM, a dc-biased tip detects the variations of local potential induced by the lateral ac voltage applied to the sample. Unlike the traditional dc and ac transport measurement, both of these techniques are sensitive to the variation of local potential (SSPM) or local voltage oscillation amplitude and phase (SIM), rather than to current. Therefore, special attention is paid to the relationship between SSPM and SIM images and data obtained from traditional impedance spectroscopy and dc transport measurements. For $BiFeO_3$ ceramics excellent agreement between the local SIM measurements and impedance spectroscopy data are demonstrated.

Comments
Copyright The American Ceramic Society. Reprinted from *Journal of the American Ceramic Society*, Volume 85, Issue 12, December 2002, pages 3011-3017.

This journal article is available at ScholarlyCommons: http://repository.upenn.edu/mse_papers/31

journal

J. Am. Ceram. Soc., **85** [12] 3011–17 (2002)

Potential and Impedance Imaging of Polycrystalline $BiFeO_3$ Ceramics

Sergei V. Kalinin, Matthew R. Suchomel, Peter K. Davies,* and Dawn A. Bonnell*

Department of Materials Science and Engineering, University of Pennsylvania, Philadelphia, Pennsylvania 19104

Electrostatic-force-sensitive scanning probe microscopy (SPM) is used to investigate grain boundary behavior in polycrystalline $BiFeO_3$ ceramics. Scanning surface potential microscopy (SSPM) of a laterally biased sample exhibits potential drops due to resistive barriers at the grain boundaries. In this technique, the tips acts as a moving voltage probe detecting local variations of potential associated with the ohmic losses within the grains and at the grain boundaries. An approach for the quantification of grain boundary, grain interior, and contact resistivity from SSPM data is developed. Scanning impedance microscopy (SIM) is used to visualize capacitive barriers at the grain boundaries. In SIM, a dc-biased tip detects the variations of local potential induced by the lateral ac voltage applied to the sample. Unlike the traditional dc and ac transport measurement, both of these techniques are sensitive to the variation of local potential (SSPM) or local voltage oscillation amplitude and phase (SIM), rather than to current. Therefore, special attention is paid to the relationship between SSPM and SIM images and data obtained from traditional impedance spectroscopy and dc transport measurements. For $BiFeO_3$ ceramics excellent agreement between the local SIM measurements and impedance spectroscopy data are demonstrated.

I. Introduction

APPLICATIONS of semiconducting oxides as chemical sensors, solar and fuel cells, and electronic ceramic devices attract significant interest to these materials.[1–3] In many cases, the macroscopic properties of ceramics are determined by the microstructure, particularly by grain boundary structure and topology. The most versatile tools for the characterization of oxide ceramics are impedance spectroscopy and dc transport measurement.[4–8] Through analysis of the frequency dependence of the amplitude and phase of a bias-induced current the major relaxation processes in the solid can be associated with individual microstructural elements. The typical applications of impedance spectroscopy differentiate grain boundary, grain interior, and electrode impedances by fitting the impedance data to corresponding equivalent circuit models. This approach addresses the average properties of a polycrystalline material and little or no information is obtained about the properties of the individual elements. Moreover, for complex (e.g., multiphase) systems the equivalent circuits rapidly become complex and nonunique. Additional complications arise in the impedance spectroscopy of ferroelectric materials in which domain walls can participate in the relaxation processes.[9] Therefore, interpretation of impedance spectra of a polycrystalline material in terms of the microstructure represents a complex problem. Finally, the correlation between atomic structure of grain boundaries and transport properties requires spatially resolved transport data. A number of approaches have been suggested to separate the impedance response of individual structural elements, such as microimpedance spectroscopy using patterned contact arrays[10–12] or studies of bicrystal samples.[13,14] Using these techniques, Fleig and Maier[15] have been able to perform impedance spectroscopy over a single grain boundary. However, this approach relies heavily on the preset contact pattern, and the maximum resolution achieved by this technique (~20 μm) is well below the resolution of microscopic techniques. Nonuniform current distribution between contacts hinders the studies of voltage-dependent properties of individual interface.[16] The small contact area inevitably leads to high contact resistance that contributes heavily to both ac and dc transport data. Specifically, as shown by Mason *et al.*, high contact resistance precludes quantitative four-probe impedance spectroscopy due to the voltage divider effect.[17,18] For dc transport measurements, contact resistance higher than the input impedance of the voltmeter precludes reliable conductivity measurements. Increasing contact resistance for small contact areas imposes a fundamental limit on local characterization of materials properties by current-based techniques.

Alternatively, spatially resolved electrostatic properties of surfaces can be addressed by variants of the scanning probe microscopy (SPM) techniques. SPM has been successfully applied to semiconductor,[19] organic,[20] and ferroelectric[21,22] surfaces, as well as to defects,[23,24] and photoinduced[25,26] and thermal phenomena[27,28] in these materials. A number of SPM studies on grain boundary related phenomena have also been reported.[29,30] However, despite a few notable exceptions, the information provided by SPM has been limited to static properties of the surfaces.[31–33] The primary limitation of all SPM techniques as applied to materials characterization stems from the fact that they are ultimately based on tip–surface interactions; therefore, SPM analysis of the lateral transport properties of material requires an additional effort.

In the present paper, a general framework for application of scanning probe microscopy to characterization of ac and dc transport properties of individual interfaces is demonstrated through an analysis of polycrystalline bismuth ferrite. $BiFeO_3$ simultaneously exhibits both ferroelectric (T_C = 830°C) and long-range antiferromagnetic G-type ordering (T_N = 370°C).[34] Because of this magnetoelectric coupling, it has been proposed that $BiFeO_3$ ceramics systems could be used to develop novel memory device applications. Extensive structural, magnetic, and electric studies of various $BiFeO_3$ solid solutions systems have been reported.[35–37] However, perhaps because of the difficulty of obtaining a single-phase material, there have been fewer reported studies of pure $BiFeO_3$. The majority of the published studies of pure $BiFeO_3$ have focused on understanding the atomic structure and complex magnetic ordering. Most of these studies have reported the existence of small impurity phases in their samples, but the impurity levels were typically deemed too low to affect the structural and magnetic studies. In contrast, the electric and dielectric properties of $BiFeO_3$, which could be strongly affected by small amounts of impurities and ferroelectric behavior, have been inadequately investigated. Our preliminary work on $BiFeO_3$ suggests that the segregation of these impurities creates resistive grain boundaries, leading to complex impedance behavior and

T. E. Mitchell—contributing editor

Manuscript No. 187454. Received September 17, 2001; approved July 10, 2002.
This work received financial support through MRSEC Grant No. NSF DMR 00-79909.

*Member, American Ceramic Society.

grain boundary barrier layer (GBBL) dielectric effects. In the present study, it is shown that SPM can be used to facilitate the understanding of the macroscopic impedance and dielectric properties by clarifying the local ac and dc transport properties of polycrystalline $BiFeO_3$ samples. Scanning surface potential microscopy (SSPM) is applied to a laterally dc-biased sample and the tip acts as a moving voltage probe detecting local potential variations associated with the ohmic losses within the grains and at the grain boundaries. A recently proposed scanning impedance microscopy (SIM) technique is used to address the ac transport properties.

II. Theoretical Development

SSPM is a well-established SPM technique that allows the local potential to be determined with submicrometer resolution. SIM is a novel scanning probe technique that allows local impedance imaging. The information provided by SSPM and SIM on laterally biased devices is summarized in Fig. 1. Quantification of dc and ac transport properties of multiple interface systems from SSPM and SIM data are considered below.

(1) dc Transport Properties by SSPM

SSPM has been successfully used to detect stray fields over Schottky double barriers in electroceramics and semiconductors and to image potential drops at laterally biased grain boundaries. Reconstruction of current–voltage properties of a single grain boundary in a bicrystal was recently illustrated.[38] The more general case of a polycrystalline sample is developed here. Assuming the series arrangement of the grains, total resistance of the sample, R_Σ, can be written as

$$R_\Sigma = R_{lc} + NR_{gi} + (N-1)R_{gb} + R_{rc} \tag{1}$$

where R_{lc} is the resistance of the left contact, R_{rc} is the resistance of the right contact, R_{gb} is the grain boundary resistance, R_{gi} is the resistance of the grain interior, and $N = n + m + 1$ is the number of the grains, n and m being the number of grains to the right and left of the investigated grain. Equation (1) can be interpreted in terms of the brick-layer model, where R_Σ is $R_{sample}S_{sample}/S_{grain}$, where R_{sample} is sample resistance, S_{grain} is average grain size, and S_{sample} is sample cross-section area. The potential drop at the individual grain boundary, $\Delta V_{gb} = V_1 - V_2$, is

$$\Delta V_{gb} = \left(\frac{R_{gb}}{R_\Sigma}\right)V \tag{2}$$

where V is the lateral dc bias. The potential drop within the grain, $\Delta V_{gi} = V_2 - V_3$, can be determined as

$$\Delta V_{gi} = \left(\frac{R_{gi}}{R_\Sigma}\right)V = \left(\frac{\mathrm{d}V}{\mathrm{d}x}\right)l \tag{3}$$

where $\mathrm{d}V/\mathrm{d}x$ is the experimentally determined potential gradient along the grain and l is the grain size. Therefore, the ratio of the potential drop at the grain boundary and in the grain interior, α, is equal to the ratio of the grain boundary and grain interior resistivities

$$\frac{\Delta V_{gb}}{\Delta V_{gi}} = \frac{R_{gb}}{R_{gi}} = \alpha \tag{4}$$

Provided that the electrode resistance is small, $R_{rc} + R_{lc} << N(R_{gb} + R_{gi})$, the total resistance can be measured directly and the grain boundary and grain interior resistances are

$$R_{gb} = \left(\frac{1}{N}\right)\left(\frac{\alpha}{\alpha+1}\right)R_\Sigma \tag{5a}$$

$$R_{gi} = \left(\frac{1}{N}\right)\left(\frac{1}{\alpha+1}\right)R_\Sigma \tag{5b}$$

This approach can also be extended to high electrode resistance. In this case, direct measurement of the surface potential close to the right electrode and close to the left electrode allows potential drops at the electrodes to be distinguished from the potential drop in the bulk and all three components of dc resistivity can be determined.

(2) ac Transport Properties by SIM

The direct application of SIM allows quantitative measurements of phase changes within the grain and grain boundaries as well as delineation of the resistive versus capacitive behavior of individual microstructural elements.

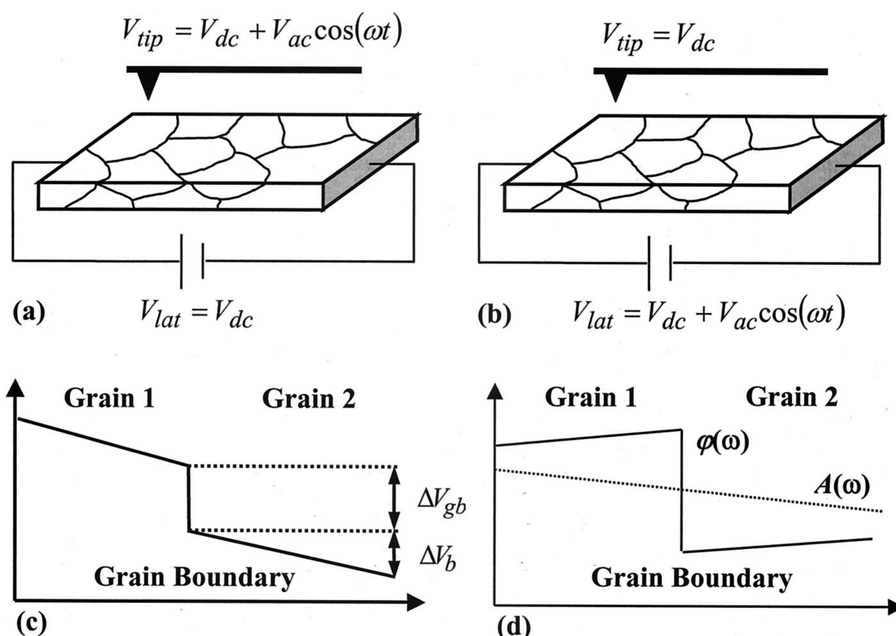

Fig. 1. Schematic diagram comparing (a) scanning surface potential microscopy (SSPM) and (b) scanning impedance microscopy (SIM). SSPM yields information on potential drops within the grains and at the grain boundaries (c), thus allowing the analysis of dc transport properties of the sample similar to 4-probe resistance measurements. SIM yields information on the local voltage amplitude and phase angle (d) and ac transport properties.

Assuming the series arrangement of the grains (Fig. 2(b)), the total impedance of the sample, Z_Σ, is

$$Z_\Sigma = Z_{lc} + N(Z_{gb} + Z_{gi}) + Z_{rc} \tag{6}$$

where Z_{lc} is the impedance of the left contact, Z_{rc} is the impedance of the right contact, Z_{gb} is the grain boundary impedance, Z_{gi} is the impedance of the grain interior, and $N = n + m + 1$ is the number of grains. Grain boundary and grain interior impedances are modeled by capacitive and resistive elements in parallel,

$$Z_{gb} = \frac{1}{1/R_{gb} + i2\pi f C_{gb}} \tag{7a}$$

$$Z_{gi} = \frac{1}{1/R_{gi} + i2\pi f C_{gi}} \tag{7b}$$

where f is frequency, R_{gb} and C_{gb} are the grain boundary resistance and capacitance, and R_{gi} and C_{gi} are the grain interior resistance and capacitance. As for the dc transport, Eq. (6) can be interpreted in terms of the brick-layer model, where measured grain boundary and bulk resistances and capacitances for the sample are scaled linearly and reciprocally by the number of grains in the cross section of the sample.

The phase change at the grain boundary is calculated from the ratio of impedances between the region to the left and to the right of the grain boundary and the ground:

$$\beta = \frac{nZ_{gb} + (n+1)Z_{gi} + Z_{rc}}{(n+1)(Z_{gb} + Z_{gi}) + Z_{rc}} \tag{8}$$

as (impedance divider effect)

$$\tan(\varphi_{gb}) = \frac{\mathrm{Im}(\beta)}{\mathrm{Re}(\beta)} \tag{9}$$

The ratio of voltage oscillation amplitudes on the left and on the right is

$$\frac{A_2}{A_1} = |\beta| \tag{10}$$

For high tip biases during SIM measurement this ratio is equal to the ratio of the tip oscillation signal (lock-in output) and is independent of the properties of the tip. Similar analysis for the grain interior and electrodes is straightforward.

It should be noted that Eqs. (1) and (6) are directly interpretable in terms of the brick-layer model. Indeed, the grain boundary and bulk impedances scale reciprocally with cross-section area; therefore, impedance ratios defined in Eqs. (4) and (8) do not depend on sample area.

It is illustrative to model the typical behavior of these values for a realistic material. Figure 3 shows impedance spectra and the SIM phase and amplitude characteristics of the grain boundary and grain interior calculated for a circuit in Fig. 2(b) with C_{gi} = 10 nF, R_{gi} = 1 kΩ, C_{gb} = 1 μF, R_{gi} = 3 kΩ, C_{lc} = 3 μF, and R_{lc} = 10 kΩ.† Calculated responses without a contact impedance contribution (generic termination) (1), including contact impedance (2), assuming only contact resistance (3), and for contact resistance R_{lc} = 100 MΩ (4) are shown. The impedance spectra exhibit two well-defined half arcs corresponding to grain boundaries and grain interior and partially overlapping electrode half arc. Modeling the SIM grain boundary phase shift shows that the phase shift is a maximum for the frequency between characteristic relaxation frequencies for the bulk and grain boundary. This frequency is further referred to as the voltage resonant frequency of the interface. The grain interior phase shift is equal to the grain boundary phase shift in magnitude and opposite in sign. The only exception is for a purely resistive circuit termination. In this case, there is an asymmetry between the grain boundary and grain interior phase shifts. It should be noted that the typical setup for SIM imaging includes current limiting resistors in the circuit and, therefore, resistive termination is usual. The grain boundary amplitude ratio is small below the resonant frequency and goes to unity above the resonant frequency. Therefore, amplitude changes are expected on the grain boundaries below the resonant frequency (dc limit), while for high frequencies grain boundaries are not associated with amplitude changes. In contrast, the grain interior amplitude ratio (i.e., local slope) in the dc limit is equal to $R_{gb}/(R_{gi} + R_{gb})$ and decreases for higher frequencies, but never achieves unity. Therefore, in the high-frequency limit the SIM amplitude is expected to exhibit uniform decay along the sample surface and grain boundary barriers are not visible in the SIM amplitude image.

This observation implies that the SIM imaging of polycrystalline ceramics will exhibit phase shifts on the interface and phase shifts of the opposite sign in the grain interior. The presence of the resistive circuit termination suppresses the latter for frequencies above the resonant frequency. At the same time, below the resonant frequency the amplitude drops at the interfaces and exhibits uniform behavior within the grains similarly to the dc potential behavior. Above the resonant frequency there is no amplitude change at the interfaces, while there is an amplitude drop within the grain that can be determined as a uniform slope.

III. Experimental Procedure

The AFM and SSPM measurements were performed with a commercial instrument (Digital Instruments Dimension 3000 NS-III) using metal-coated tips ($l \approx 225$ μm, resonant frequency ~ 60 kHz, $k \approx 1$–5 N/m). To perform SIM,[39] the AFM was additionally

†Resistance and capacitance of contacts on the left do not influence the voltage phase angle shift and voltage oscillation amplitude ratio across the interface.

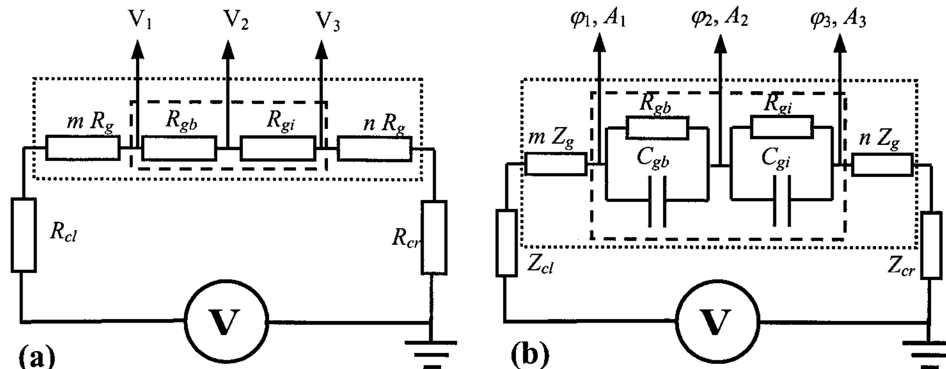

Fig. 2. Equivalent circuits for SSPM under lateral bias (a) and SIM (b) and the origins of the measured signal.

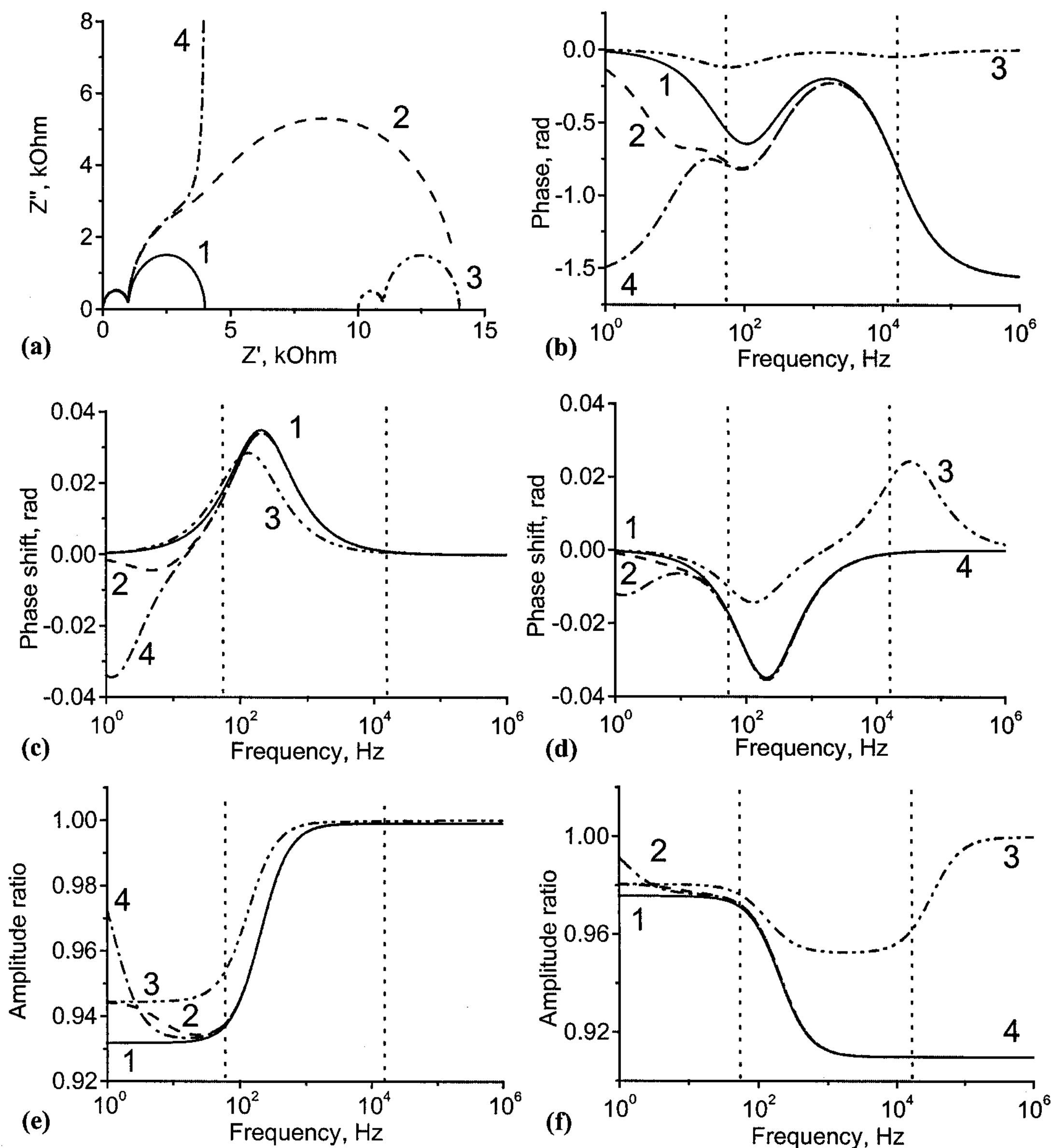

Fig. 3. Calculated Cole–Cole plots (a), impedance phase angle versus frequency (b), SIM phase shifts at the grain boundary (c) and within the grain (d), and SIM amplitude ratios at the grain boundary (e) and within the grain (f), for a circuit without a contact contribution (generic termination) (1), with a contact contribution (2), with purely resistive termination (3), and with high-resistance contacts (4). Parameters are given in the text. The impedance phase angle characterizes the phase lag between the ac voltage and current in the sample, while the voltage phase angle (c,d) describes the phase of voltage oscillation along the surface.

equipped with a function generator and lock-in amplifier (DS340, SRS 830, Stanford Research Systems) as described elsewhere.[38] The lift height for the interleave scans in the SSPM and SIM was usually 100 nm; the scan rate varied from 0.5 Hz for large scans (~60 μm) to 1 Hz for smaller scans (~10 μm). The driving voltage V_{ac} in the interleave scan was 5 V for SSPM and 10 V for SIM. To reduce the effect of drift the images were acquired with the grain boundaries preferentially oriented along the slow scan axis. Topographical images were processed by line flattening.[40] SSPM and SIM images were processed only by constant background subtraction. Phase, amplitude, and potential profiles were obtained by averaging the SIM and SSPM images along the slow scan axis.

The $BiFeO_3$ sample was prepared using a modified version of the procedure first described by Achenbach *et al.*[41] The dried oxide reagents, Bi_2O_3 (99.999% pure, Cerac Incorporated) and Fe_2O_3 (99.99% pure, Fisher Scientific), were mixed together in a 5% Bi_2O_3-rich molar ratio and ball-milled for 12 h. This excess of Bi_2O_3 was sufficient to suppress the formation of the often-reported $Bi_2Fe_4O_9$ impurity. The sample was heated twice at 815°C for 4 h with ball milling in between. Excess Bi_2O_3 was removed via a two-step leaching process using first 3.25*M* then 1.75*M* HNO_3, followed by several deionized water rinses and drying. The resultant powder was further ball-milled and isostatically pressed into a pellet at 500 MPa. Sintering was conducted at 830°C for 3 h, followed by annealing for 10 h at 500°C. X-ray diffraction analysis of both powder and pellet showed single-phase $BiFeO_3$. The pellet was cut into a rectangular shape, and silver paint (ST1601-14, Heraeus Inc.) was used to create parallel electrodes on the sample. Macroscopic impedance analysis was preformed with an HP 4284A LCR meter over the range of 20 Hz to 1 MHz.

IV. Results and Discussion

(1) SSPM under Lateral Bias

The surface topography and surface potential at a $BiFeO_3$ surface under different bias conditions are shown in Fig. 4. The

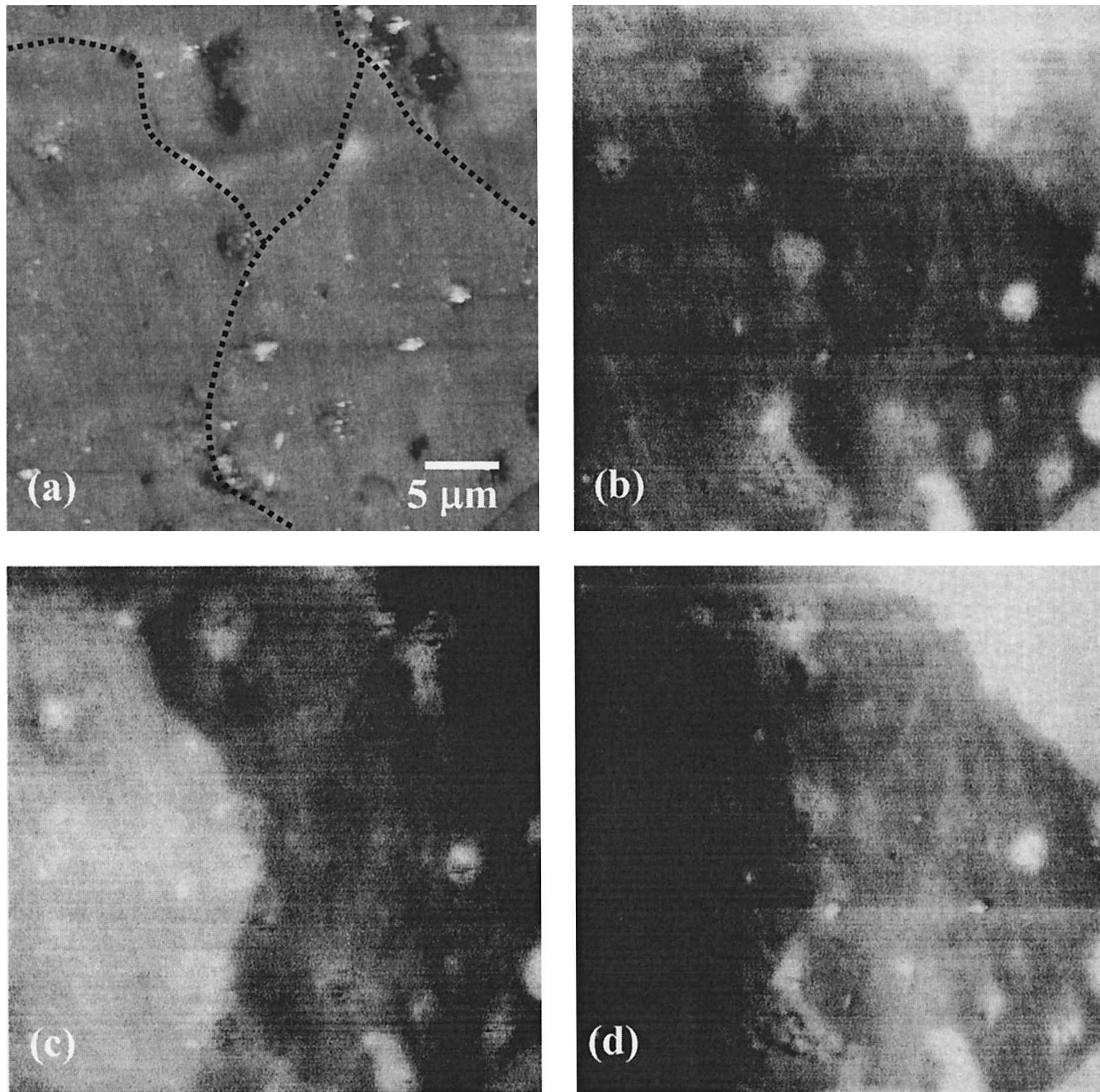

Fig. 4. Surface topography (a), surface potential of the grounded surface (b), and surface under lateral bias of 10 V (c) and −10 V (d). Significant potential variations on the grounded surface are due to the variations in surface polarization charge density induced by the ferroelectric domain structure of the sample. Application of the lateral bias results in potential drops at the grain boundaries; domain related potential features are bias independent. Scale is 200 nm (a), and 50 mV (b–d).

topographic image exhibits a number of spots due to contaminants and depressions due to inter- and intragranular pores. Grain boundaries can be seen due to selective polishing of grains with different orientations. The surface potential of the grounded $BiFeO_3$ surface exhibits large-scale potential variations due to ferroelectric domains and surface contaminants. On application of a 10 V lateral bias the potential drops at the grain boundaries become evident (Fig. 4(c)). The contrast inverts on application of a bias of opposite polarity (Fig. 4(d)). Note that the potential features related to ferroelectric polarization are independent of the applied bias. Ramping the dc bias across the sample has shown that the potential drop at the interface is linear in external bias and the grain boundaries exhibit ohmic behavior for small biases ($\Delta V_{gb} < 50$ mV)).

(2) *ac Transport by SIM*

The surface topography, SIM phase images at 20 and 70 kHz and the SIM amplitude image at 70 kHz of the same region are shown in Fig. 5. Note that the phase images exhibit well-defined phase shifts at the grain boundaries, while the amplitude image shows a uniform decrease of amplitude across the surface. Positive phase shifts at the grain boundary and a negative phase shift in the bulk are clearly observed in agreement with theoretical arguments. For higher frequencies phase shifts in the grain interior are not observed because of the resistive component in the experimental circuit. At the same time, the amplitude decreases linearly in the direction of current flow, indicating that the experimental frequency range (10–100 kHz) is above the resonant frequency of the interface. To quantify the frequency dependence of the grain boundary phase shift, the latter was determined for a series of images collected at 10 kHz steps. The analysis in the vicinity of the resonant frequency of the cantilever (60 kHz) is complex because of a force-gradient induced resonant frequency shift and associated nonlinear phase behavior. Therefore, tip-surface phase lag is not constant in the vicinity of cantilever resonance. To relate the SIM phase shift to the material properties, the latter were independently determined by impedance spectroscopy and the corresponding spectra are shown in Fig. 6. From the impedance spectroscopy data, the average grain boundary resistivity and capacitance are estimated as $R_{gb} = 116$ kΩ·cm and $C_{gb} = 7.6$ nF/cm, while the grain interior resistivity and capacitance are $R_{gi} = 812$ Ω·cm and $C_{gi} = 7$ pF/cm. It should be noted that two RC elements provide a relatively poor description of the high-frequency region of the experimental impedance spectra;

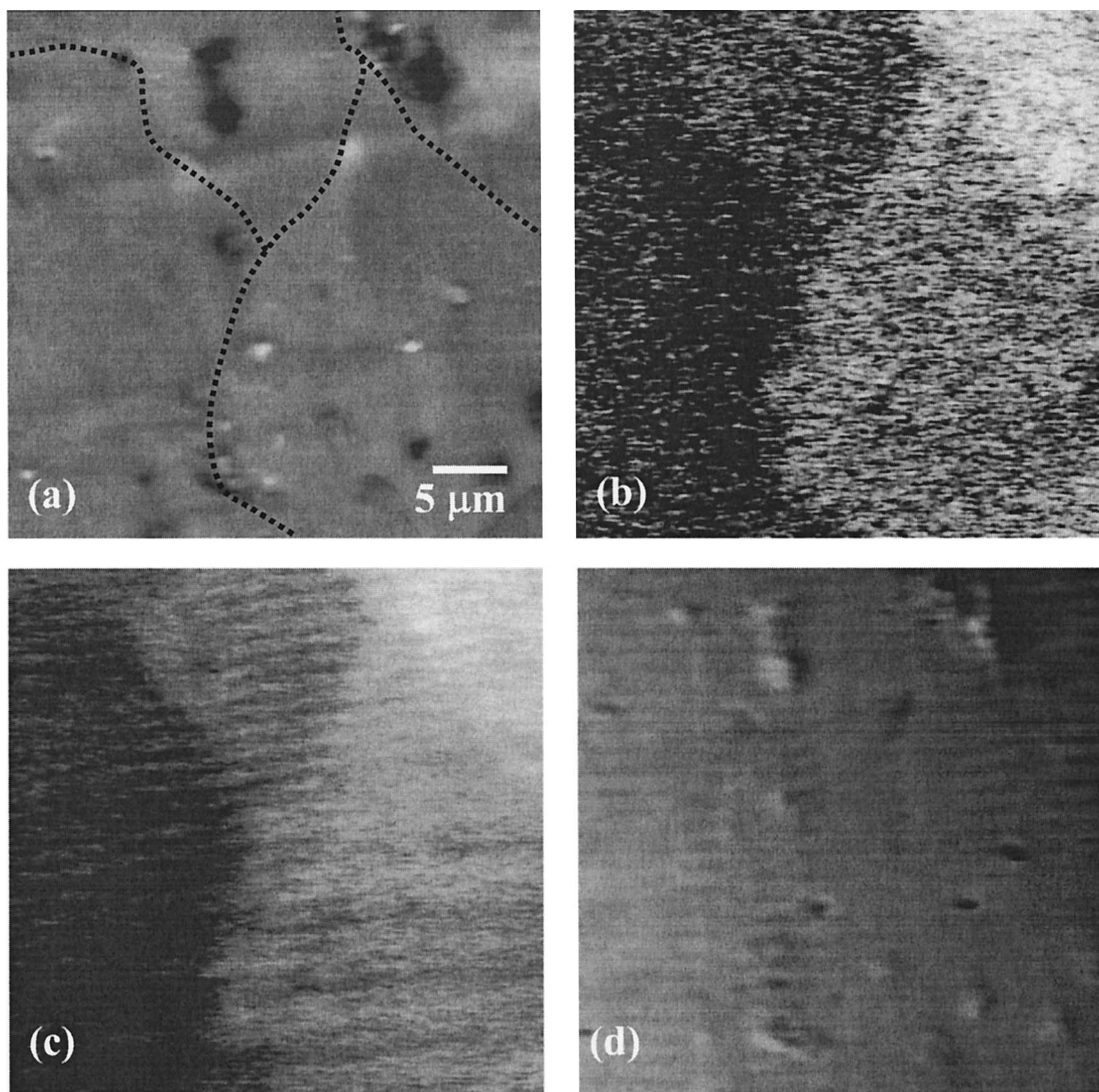

Fig. 5. Surface topography (a), SIM phase image at 30 kHz (b) and 70 kHz (c), and SIM amplitude image at 70 kHz (d) of the same region. The voltage phase angle changes abruptly at the interfaces. At least one of the interfaces is not associated with a significant potential drop in the dc mode. The amplitude image exhibits a linear decay of oscillation amplitude indicative of uniform losses. Scale is 200 nm (a), 0.2° (b,c).

the properties of the grain boundary component are well-defined, whereas bulk properties can be determined only approximately. Figure 7 shows the calculated grain boundary phase shift versus frequency dependence as compared with experimental SIM data. The only free parameter in the calculations is the effective grain number. The best fit is obtained for $n = 210$ grains, which is comparable with grain number $N \sim 70$ estimated from the grain size (~20–30 μm) and the distance between the measurement point and the left contact (~1–2 mm). The discrepancy between the two is due to the uncertainty in the bulk resistance and variation in grain boundary properties and orientation. Note the excellent agreement between phase angle frequency dependencies obtained from local measurements and impedance spectroscopy.

V. Conclusions

Scanning probe imaging of electroactive interfaces in ceramic materials and their relationship with conventional 4-probe resistance and impedance spectroscopy measurements have been discussed. Both scanning surface potential microscopy (SSPM) of laterally biased devices and scanning impedance microscopy (SIM) are based on the local detection of surface potential or voltage oscillation amplitude and phase angle by the SPM tip. These techniques permit the local properties to be determined with aresolution of ~100 nm. A noncontact detection mechanism implies that the probe impedance does not contribute to the measured potential, voltage phase, and amplitude. The utility of these techniques for material characterization was illustrated on a sample of polycrystalline $BiFeO_3$. SSPM of the grounded surface revealed significant potential variations due to ferroelectric polarization. Application of a lateral bias to the electroded sample demonstrated potential drops due to resistive barriers at the grain boundaries; however, quantitative analysis of the SSPM data was precluded by a ferroelectric contribution to the measured potential. SIM phase images of the same region clearly exhibited phase shifts at the interfaces. SIM amplitude images indicated a uniform decrease of the voltage oscillation amplitude across the sample, in agreement with theoretical arguments. At the same time, ferroelectric domain boundaries did not contribute to the SIM image, thus allowing unambiguous correlation of impedance spectra with electroactive grain boundaries. A theoretical model for the quantification of SIM measurements based on the voltage divider effect was developed and used to simulate the SIM phase behavior. For $BiFeO_3$ ceramics excellent agreement between local SIM measurements and impedance spectroscopy data was found.

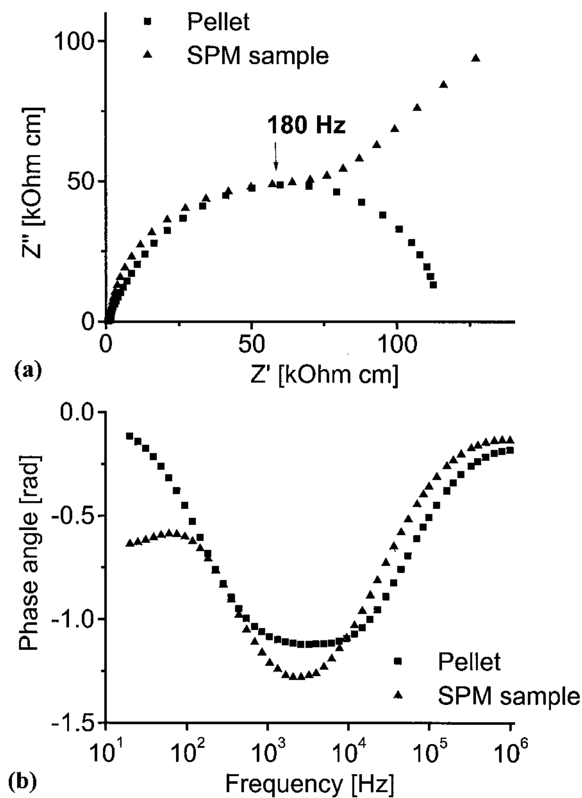

Fig. 6. (a) Cole–Cole plots of as-prepared $BiFeO_3$ pellets and the rectangular sample used for scanning probe microscopy studies. (b) Frequency dependence of the phase angle for the same samples.

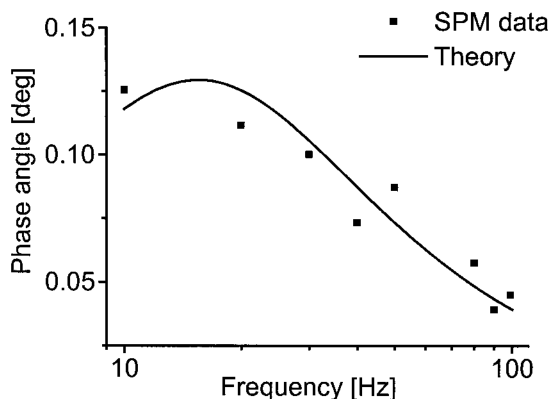

Fig. 7. Experimental SIM phase shift across the interface and theoretical curve calculated from the impedance spectra of the sample.

References

[1]L. L. Hench and J. K West (eds.), *Principles of Electronic Ceramics*. Wiley-Interscience, New York, 1990.

[2] R. Buchanan (ed.), *Ceramic Materials for Electronics*. Marcel Dekker, New York, 1991.

[3]L. M. Levinson (ed.), *Electronic Ceramics: Properties, Devices and Applications*. Marcel Dekker, New York, 1988.

[4]J. R. Macdonald (ed.), *Impedance Microscopy: Emphasizing Solid Materials and Systems*. Wiley, New York, 1987.

[5]B.-S. Hong, S. J. Ford, and T. O. Mason, "Equilibrium Electric Property Measurements in Electroceramics," *Key Eng. Mater.*, **125–126**, 163–85 (1997).

[6]S. P. Jiang, J. G. Love, and S. P. S. Badwal, "Electrochemical Techniques in Studies of Solid-State Ionic Conductors," *Key Eng. Mater.*, **125–126**, 81–132 (1997).

[7]N. S. Hari, P. Padmini, and T. R. N. Kutty, "Complex Impedance Analyses of *n*-$BaTiO_3$ Ceramics Showing Positive Temperature Coefficient of Resistance," *J. Mater. Sci.: Materials Electron.*, **8**, 15–22 (1997).

[8]R. Waser and R. Hagenbeck, "Grain Boundaries in Dielectric and Mixed-Conducting Ceramics," *Acta Mater.*, **48**, 797–825 (2000).

[9]C. Elissalde and J. Ravez, "Ferroelectric Ceramics: Defects and Dielectric Relaxation," *J. Mater. Chem.*, **11**, 1957 (2001).

[10]J. Fleig, S. Rodewald, and J. Maier, "Microcontact Impedance Measurements of Individual Highly Resistive Grain Boundaries: General Aspects and Application to Acceptor-Doped $SrTiO_3$," *J. Appl. Phys.*, **87**, 2372–81 (2000).

[11]S. H. Kim, J. H. Suh, J. G. Park, and Y. Kim, "Influence of Defect Segregation on the Electrical Properties of Nb-Doped $SrTiO_3$ Grain Boundary Layer," *Jpn. J. Appl. Phys.*, **39**, 1788–95 (2000).

[12]A. S. Skapin, J. Jamnik, and S. Pejovnik, "Grain Boundary Conductance in AgCl Gained by Micro-contact Impedance Spectroscopy," *Solid State Ionics*, **133**, 129–38 (2000).

[13]J. H. Hwang, K. D. Johnson, T. O. Mason, and V. P. Dravid, "Single Grain Boundary Characterization of Nb-Doped $SrTiO_3$ Bicrystals Using ac Four-Point Impedance Spectroscopy," *Appl. Phys. Lett.*, **76**, 2621–23 (2000).

[14]S. Tanaka and K. Takahashi, "Direct Measurements of Voltage–Current Characteristics of Single Grain Boundary of ZnO Varistors," *J. Eur. Ceram. Soc.*, **19**, 727–30 (1999).

[15]S. Rodewald, J. Fleig, and J. Maier, "Microcontact Impedance Spectroscopy at Single Grain Boundaries in Fe-Doped $SrTiO_3$ Polycrystals," *J. Am. Ceram. Soc.*, **84**, 521–30 (2001).

[16]J. Fleig, "Interfacial Impedance in Electroceramics: The Effects of Inhomogeneous Current Distributions," *Ceram. Trans.*, **109**, 31–40 (2000).

[17]J.-H. Hwang, K. S. Kirkpatrick, T. O. Mason, and E. J. Garboczi, "Experimental Limitations in Impedance Spectroscopy: Part IV, Electrode Contact Effects," *Solid State Ionics*, **98**, 93–104 (1997).

[18]D. D. Edwards, J.-H. Hwang, S. J. Ford, and T. O. Mason, "Experimental Limitations in Impedance Spectroscopy: Part V, Apparatus Contributions and Corrections," *Solid State Ionics*, **99**, 85–93 (1997).

[19]M. Tanimoto and O. Vatel, "Kelvin Probe Force Microscopy for Characterization of Semiconductor Devices and Processes," *J. Vac. Sci. Technol*, **B14**0, 1547–51 (1996).

[20]M. Fujihira, "Kelvin Probe Force Microscopy of Molecular Surfaces," *Annu. Rev. Mater. Sci.*, **29**, 353–80 (1999).

[21]X. Q. Chen, H. Yamada, T. Horiuchi, K. Matsushige, S. Watanabe, M. Kawai, and P. S. Weiss, "Surface Potential of Ferroelectric Thin Films Investigated by Scanning Probe Microscopy," *J. Vac. Sci. Technol.*, **B17**0, 1930–34 (1999).

[22]T. Tybell, C. H. Ahn, and J.-M. Triscone, "Ferroelectricity in Thin Perovskite Films," *Appl. Phys. Lett.,* **75**, 856–58 (1999).

[23]P. M. Bridger, Z. Z. Bandic, E. C. Piquette, and T. C. McGill, "Measurement of Induced Surface Charges, Contact Potentials, and Surface States in GaN by Electric Force Microscopy," *Appl. Phys. Lett.*, **74**, 3522–24 (1999).

[24]Q. Xu and J. W. P. Hsu, "Electrostatic Force Microscopy Studies of Surface Defects on GaAs/Ge Films," *J. Appl. Phys.*, **85**, 2465–72 (1999).

[25]A. Chavez-Pirson, O. Vatel, M. Tanimoto, H. Ando, H. Iwamura, and H. Kanbe, "Nanometer-Scale Imaging of Potential Profiles in Optically Excited n-i-p Heterostructure Using Kelvin Probe Force Microscopy," *Appl. Phys. Lett.*, **67**, 3069–71 (1995).

[26]T. Meoded, R. Shikler, N. Fried, and Y. Rosenwaks, "Direct Measurement of Minority Carriers Diffusion Length Using Kelvin Probe Force Microscopy," *Appl. Phys. Lett.*, **75**, 2435–37 (1999).

[27]S. V. Kalinin and D. A. Bonnell, "Dynamic Behavior of Domain-Related Topography and Surface Potential on the $BaTiO_3$ (100) Surface by Variable Temperature Scanning Surface Potential Microscopy," *Z. Metallkd.*, **90**, 983–89 (1999).

[28]E. Z. Luo, Z. Xie, J. B. Xu, I. H. Wilson, and L. H. Zhao, "*In Situ* Observation of the Ferroelectric–Paraelectric Phase Transition in a Triglycine Sulfate Single Crystal by Variable-Temperature Electrostatic Force Microscopy," *Phys. Rev.*, **B61**, 203–206 (2000).

[29]B. D. Huey, D. Lisjak, and D. A. Bonnell, "Nanometer-Scale Variations in Interface Potential by Scanning Probe Microscopy," *J. Am. Ceram. Soc.*, **820**, 1941–44 (1999).

[30]Q. Xu and J. W. P. Hsu, "Direct Measurement of Surface Defect Level Distribution Associated with GaAs Antiphase Boundaries," *Phys. Rev. Lett.*, **820**, 612–15 (1999).

[31]S. V. Kalinin and D. A. Bonnell, "Surface Potential at Surface-Interface Junctions in $SrTiO_3$ Bicrystals," *Phys. Rev.*, **B62**, 10419–30 (2000).

[32]B. D. Huey and D. A. Bonnell, "Spatially Localized Dynamic Properties of Individual Interfaces in Semiconducting Oxides," *Appl. Phys. Lett.*, **760**, 1012–14 (2000).

[33]D. A. Bonnell and S. V. Kalinin; in Solid State Phenomena Series, *Polycrystalline Semiconductors VI —Bulk Materials, Thin Films and Devices*. Edited by O. Bonnaud, T. Mohammed-Brahim, H. P. Strunk, and J. H. Werner. Scitech Publishing, Uettikon am See, Switzerland, in press.

[34]P. Fischer, M. Polomska, I. Sosnowska, and M. Szymanski, "Temperature Dependence of the Crystal and Magnetic Structures of $BiFeO_3$," *J. Phys. C: Solid State Phys.*, **13**, 1931–40 (1980).

[35]M. M. Kumar, A. Srinivas, S. V. Suryanarayana, and T. Bhimasankaram., "Dielectric and Impedance Studies on $BiFeO_3$–$BaTiO_3$ Solid Solutions," *Phys. Status Solidi A*, **165**, 317–26 (1998).

[36]M. Polomska, W. Kaczmarek, and Z. Pajak, "Electric and Magnetic Properties of $Bi_{1-x}La_xFeO_3$ Solid Solutions," *Phys. Status Solidi A*, **23**, 567–74 (1974).

[37]J. B. MacChesney, J. J. Jetzt, J. F. Potter, H. J. Williams, and R. C. Sherwood, "Electric and Magnetic Properties of the System $SrFeO_3$–$BiFeO_3$," *J. Am. Ceram. Soc.*, **49**, 644–47 (1966).

[38]S. V. Kalinin and D. A. Bonnell, "Scanning Impedance Microscopy of Electroactive Interfaces," *Appl. Phys. Lett.*, **78**, 1306–308 (2001).

[39]D. A. Bonnell and S. V. Kalinin, "Scanning Impedance Microscopy of Electroactive Interfaces," UPN-3964/N2478.

[40]"Command Reference Manual," Digital Instruments, Santa Barbara, CA, 1997.

[41]G. D. Achenbach, W. J. James, and R Gerson, "Preparation of Single-Phase Polycrystalline $BiFeO_3$," *J. Am. Ceram. Soc.*, **50**, 437 (1967). □